HHS Public Access

Author manuscript

Biomaterials. Author manuscript; available in PMC 2021 November 01.

Published in final edited form as:

Biomaterials. 2020 November ; 258: 120267. doi:10.1016/j.biomaterials.2020.120267.

NIR fluorescence for monitoring *in vivo* scaffold degradation along with stem cell tracking in bone tissue engineering

Soon Hee Kim[a,e,1], **Ji Hoon Park**[a,b,1], **Jin Seon Kwon**[a,b], **Jae Gu Cho**[a,c], **Kate G. Park**[d], **Chan Hum Park**[e], **James J. Yoo**[a], **Anthony Atala**[a], **Hak Soo Choi**[d,***], **Moon Suk Kim**[b,**], **Sang Jin Lee**[a,*]

[a]Wake Forest Institute for Regenerative Medicine, Wake Forest School of Medicine, Medical Center Boulevard, Winston-Salem, NC 27157, USA

[b]Department of Molecular Science and Technology, Ajou University, Suwon 443-759, Republic of Korea

[c]Department of Otolaryngology-Head and Neck Surgery, Korea University College of Medicine, Guro-dong 80, Guro-gu, Seoul 152-703, Republic of Korea

[d]Gordon Center for Medical Imaging, Department of Radiology, Massachusetts General Hospital and Harvard Medical School, Boston, MA 02114, USA

[e]Nano-Bio Regenerative Medical Institute, College of Medicine, Hallym University, Chuncheon 24252, Republic of Korea

Abstract

Stem cell-based tissue engineering has the potential to use as an alternative for autologous tissue grafts; however, the contribution of the scaffold degradation along with the transplanted stem cells to *in vivo* tissue regeneration remains poorly understood. Near-infrared (NIR) fluorescence imaging has great potential to monitor implants while avoiding autofluorescence from the adjacent host tissue. To utilize NIR imaging for *in vivo* monitoring of scaffold degradation and cell

* sjlee@wakehealth.edu (S. J. Lee). ** moonskim@ajou.ac.kr (M. S. Kim). *** hchoi12@mgh.harvard.edu (H. S. Choi).

[1]These authors contributed equally.

CRediT Author Statement

Soon Hee Kim: Methodology, Formal Analysis, Investigation, Writing – Original Draft, Visualization **Ji Hoon Park:** Methodology, Investigation, Writing – Original Draft **Jin Seon Kwon:** Methodology, Investigation **Jae Gu Cho:** Investigation **Kate G. Park:** Investigation **Chan Hum Park:** Formal Analysis **James J. Yoo:** Methodology, Resources, Funding Acquisition **Anthony Atala:** Resources, Funding Acquisition **Hak Soo Choi:** Conceptualization, Methodology, Resources, Writing – Review & Editing, Funding Acquisition **Moon Suk Kim:** Conceptualization, Methodology, Resources, Writing – Review & Editing, Supervision, Project Administration, Funding Acquisition **Sang Jin Lee:** Conceptualization, Methodology, Formal Analysis, Resources, Writing – Review & Editing, Visualization, Supervision, Project Administration, Funding Acquisition

Declaration of interests

The authors declare that they have no known competing financial interests or personal relationships that could have appeared to influence the work reported in this paper.

Appendix A. Supplementary data

Supplementary data to this article can be found online at

Data availability

The data generated or analyzed during this study are available from the corresponding authors on reasonable request.

tracking, we synthesized 800-nm emitting NIR-conjugated PCL-*ran*-PLLA-*ran*-PGA (ZW-PCLG) copolymers with three different degradation rates and labeled 700-nm emitting lipophilic pentamethine (CTNF127) on the human placental stem cells (CT-PSCs). The 3D bioprinted hybrid constructs containing the CT-PSC-laden hydrogel together with the ZW-PCLG scaffolds demonstrate that NIR fluorescent imaging enables tracking of *in vivo* scaffold degradation and stem cell fate for bone regeneration in a rat calvarial bone defect model. This NIR-based monitoring system can be effectively utilized to study cell-based tissue engineering applications.

Keywords

NIR fluorescence; Imaging; Stem cells; Scaffold; Biodegradation; Tissue engineering

1. Introduction

Due to limited donor tissue or organ availability for transplantation, the demand for developing cell-based bioengineered tissues has rapidly risen [1, 2]. This strategy attempts to create implantable functional tissue constructs by combining patients' own cells with highly porous natural and/or synthetic polymeric scaffolds. Since these scaffolds serve as a template that supports the initial structural integrity and mechanical stability, as well as cellular interaction, the *in vivo* degradation behavior of the scaffolds during neo-tissue formation in the tissue-engineered constructs must be controlled for successful outcomes [3, 4]. The tissue-engineered constructs should be maintained their structural integrity, while the scaffold is gradually replaced by a newly formed tissue. Therefore, a better understanding of the *in vivo* scaffold degradation is significant in the scaffold design and fabrication for tissue engineering applications.

Recent progress in stem cell-based tissue engineering raises hope for the development of alternatives that can replace the need for autologous tissue grafts [5–7]. Stem cells can differentiate into multiple cell types and hold a great therapeutic promise as a cell source to promote tissue regeneration while maintaining the immunomodulation properties after transplantation [8–10]. However, the therapeutic effect and regenerative mechanism of the stem cell-based approaches are not fully understood. Determining the fate of transplanted cells is an important step in estimating a translational therapeutic method using cell-based tissue engineering strategies.

Molecular imaging modalities such as computed tomography (CT) [11–13], magnetic resonance imaging (MRI) [14, 15], positron emission tomography (PET) [16], and single-photon emission computed tomography (SPECT) [17] have been attempted to noninvasively monitor the transplanted cells [11, 14–17], scaffold degradation behavior [12], and tissue formation [13] after transplantation. Optical fluorescence imaging techniques have also been utilized for monitoring *in vivo* scaffold degradation [18–20] due to high-throughput screening for a target, high sensitivity, and a wide range of affordable experimental formats; however, the *in vitro* results may be difficult to reflect *in vivo* biodegradation behavior of the implanted scaffolds because of the physicochemical and optical instability of the visible wavelength fluorophores, as well as endogenous tissue autofluorescence [21]. To overcome

these limitations, we previously demonstrated a near-infrared (NIR)-functionalized collagen-based scaffold enabled to observe its degradation behavior *in vitro* and *in vivo* by employing invisible NIR fluorescence [22]. More importantly, we were able to quantify the *in vivo* degradation rate of implanted NIR-labeled scaffolds over 30 days of the implantation. Unlike UV-visible fluorescence, NIR fluorescence provides relatively high spatial and temporal resolution [23–25] and outperforms traditional UV-visible imaging with deeper tissue penetration and minimum tissue absorption, scattering, and autofluorescence [26–28].

In this study, we aim to investigate the relationship between the scaffold degradation and tissue regeneration in the stem cell-based tissue engineering using a dual-channel NIR fluorescence imaging system (700 nm for cells and 800 nm for polymeric scaffolds). We hypothesize that this dual-channel NIR fluorescence imaging can be utilized for noninvasively monitoring the *in vivo* degradation of implanted scaffolds and tracing transplanted cells after the construct retrieval. To achieve this, we first designed and synthesized NIR fluorophore- conjugated copolymers as scaffold materials with presenting different degradation rates by controlling the composition ratio of ε-caprolactone (CL), lactide (LA), and glycolide (GA). In order to avoid any effects from the scaffold geometry such as pore morphology, pore size, and porosity, we utilized our three-dimensional (3D) printing capability [2] to fabricate cell-laden hybrid tissue constructs for the study. Lastly, we validated these bioprinted tissue constructs containing NIR-labeled stem cells (700 nm) and NIR-functionalized PCLG copolymers (800 nm) in a rat calvarial bone defect model. Fig. 1 shows the schematic diagram of the NIR imaging system to noninvasively monitor the scaffold degradation along with immunofluorescence for trafficking the stem cell fate for bone regeneration.

2. Experimental procedures

2.1. Synthesis of NH_2-functionalized PCL-ran-PLLA-ran-PGA (PCLG) copolymers

Three PCLG copolymers with different ratios of monomers were synthesized to control the degradation rates. The 2-chlorocyclohexanone and ε-caprolactone (CL) were purchased from TCI Co., LTD. (Tokyo, Japan), and CL was purified by distillation with calcium hydride (CaH_2) under reduced pressure (150 kPa). L-lactide (LA) and glycolide (GA) were obtained from Boehringer Ingelheim (Ingelheim, Germany) and recrystallized twice in ethyl acetate. Methoxy polyethylene glycol (MPEG, Mn = 750 g/mol), stannous octoate [$Sn(Oct)_2$], and meta-chloroperoxybenzoic acid (mCPBA, 77%) were used as initiator, catalyst, and oxidation reagent, respectively. All chemical reagents were obtained from Millipore Sigma (St. Louis, MO) unless stated otherwise.

Three grams of 2-chlorocyclohexanone (22.6 mmol) was dissolved in 30 ml of dichloromethane, and mCPBA (7.6 g, 44.1 mmol) was added to the solution at room temperature. The reaction was conducted for 24 h. Then, the insoluble part of the reaction was removed by filtering, and the solution was washed three times with a saturated $NaHCO_3$ solution, brine, and DI water, respectively. The organic layer was treated with magnesium sulfate ($MgSO_4$) to remove water, and the remaining organic layer was evaporated under the reduced pressure. The isomeric materials, α-chloro-ε-caprolactone and ε-chloro-ε-caprolactone, were obtained from the crude mixture using silica column chromatography

(ThermoFisher Scientific, Waltham, MA) with dichloromethane as a mobile phase. Thereafter, isomers were separated using silica gel column chromatography and eluted in *n*-hexane:ethyl acetate at a ratio of 7:3 (v/v).

The molecular weight (Mw) and the dispersity (Đ) of the PCLG copolymers were measured using gel permeation chromatography (GPC) (YL9170RI detector) (YL Instruments, Anyang-si, Gyeonggi-do, Korea) with three columns (Shodex K-802, K-803, and K-804 polystyrene gel columns) at 40°C by polystyrene calibration and chloroform as an eluent at a flow rate of 1.0 ml/min to measure the molecular weight (Mw) and the dispersity (Đ) of the PCLG copolymers [29].

MPEG (0.016g, 0.021 mmol) and toluene (80 ml) were placed into a round-bottom flask. Water was removed by azeotropic distillation with toluene at 130°C using a Dean-Stark apparatus, and the final volume of toluene was 30 ml. CL (2.56 g, 22.4 mmol), CL-Cl (0.24, 1.6 mmol), LA (6.93 g, 48.1 mmol), and GA (0.93 g, 8.0 mmol) were added to the MPEG solution in toluene under the nitrogen atmosphere at room temperature, and then 0.3 ml of 0.1 M stannous octoate in toluene was added. After stirring for 24 h at 160° C, the reaction solution was added to a solvent mixture of *n*-hexane and ethyl ether (4:1, v/v) to precipitate the synthesized copolymers. Solids were separated by decantation, redissolved in dichloromethane, and filtered through a cellulose filter. The upheaped solution was dried using a rotary evaporator under vacuum. The molecular weights of the Cl-PCLG-1, Cl-PCLG-2, and Cl-PCLG-3 copolymers were measured using ^{1}H-NMR (300 MHz, Bruker Avance, Karlsruhe, Germany) by comparing the methylene proton signal of PCL at δ = 2.31 ppm, the methylene proton signal of PLLA at δ = 5.15 ppm, and the methylene proton signal of PGA at δ = 4.81 ppm, respectively, to the proton signals of MPEG (standard, 750 g/mol) at δ = 3.62 ppm.

Chloro-PCLG (10 g, 0.02 mmol) was dissolved *N,N*-dimethylformamide (DMF) in a round-bottom flask, and sodium azide (0.3 g, 4.6 mmol) was added and stirred at 70° C for 24 h for the nucleophilic substitution of chloride with an azide group. After 24 h, the solution was poured into a solvent mixture of n-hexane, ethyl ether, and methanol (45:45:10, v/v/v) to precipitate N_3-PCLGs. After precipitation, the supernatant was decanted from the beaker, and the solids were dissolved in DCM, filtered, and dried using a rotary evaporator and a vacuum drying oven. Synthesized N_3-PCLGs (10 g, 0.02 mmol) was dissolved in tetrahydrofuran (THF) in a flask, triphenylphosphine (PPh_3, 0.84g, 3.2 mmol) was added, and the mixture was stirred for 20 h at room temperature. After 20 h, deionized water (DW) was added to the reaction to hydrogenate the reactant for 4 h. After the reaction, the solution was poured into a solvent mixture composed of n-hexane, ethyl ether, and methanol (45:45:10, v/v/v) to precipitate the reaction products. After removing the solvent, solidified NH_2-PCLG was redissolved in DCM and dried via rotary evaporation and drying under vacuum. Azide and amide groups on the polymers were measured by FT-IR using a Thermo Nicolet 6700 spectrometer (Thermo Electron Corporation, Runcorn, UK). The glass transition temperature (T_g) was determined using differential scanning calorimetry (DSC; Q1000, TA Instruments, Eschborn, Germany) performed from −80 to 200°C at a heating rate of 5°C/min in a nitrogen atmosphere.

2.2. ZW800–1C conjugation to PCLG copolymers

The 800-nm NIR fluorescence emitting ZW800–1C was synthesized as previously reported [30]. ZW800–1C was activated with NHS and conjugated to NH_2-PCLGs [31]. Two equivalents of dipyrrolidino(*N*-succinimidyloxy)carbenium hexafluorophosphate in dimethyl sulfoxide (DMSO) were mixed with 5 equivalents of diisopropylethylamine at room temperature in the dark under agitation for 3 h. Then, the reaction mixture was precipitated with an excess of ethyl acetate. The precipitate was washed with a 1:1 mixture of ethyl acetate and acetone and dried overnight under vacuum. The primary amines on the NH_2-PCLG copolymers were conjugated with the ZW800–1C NHS ester at 1:0.01–1:2 (PCLG:ZW800–1C) molar ratios in PBS at pH 8.0 [32]. The unconjugated fluorophores were thoroughly rinsed using Bio-Scale Mini Bio-Gel P-6 Desalting columns (Bio-Rad Laboratories, Hercules, CA). The labeling ratio was calculated from the ratio of extinction coefficients between the PCLG copolymer and ZW800–1C fluorophores using a spectrophotometer (Ocean Insight, Largo, FL). The optical properties of ZW800–1C and the fluorophore quantity conjugated to the PCLG copolymers were measured using a fluorimeter at 770 nm excitation and 790 nm emission. The ZW800–1C-conjugated PCLG copolymers (ZW-PCLGs) were confirmed visually by Pearl® Impulse (800-nm channel, LI-COR Biosciences, Lincoln, NE, USA). We synthesized three ZW800–1C-conjugated PCLG copolymers with different monomer ratios: ZW-PCLG-1, ZW-PCLG-2, and ZW-PCLG-3.

2.3. 3D bioprinting of ZW-PCLG copolymers

To fabricate the ZW-PCLG scaffolds, our integrated tissue-organ printing (ITOP) system that contains a 3-axis stage and controller with multiple dispensing modules was used [33]. The ZW-PCLG copolymer was loaded in a customized metal syringe with a heating unit. The metal syringe with ZW-PCLGs was heated to 82.5°C for ZW-PCLG-1, 105°C for ZW-PCLG-2, and 100°C for ZW-PCLG-3 during the printing process. The molten ZW-PCLGs were extruded via a 300-μm cone-shaped metal nozzle at 200 kPa for ZW-PCLG-1, 500 kPa for ZW-PCLG-2, and 600 kPa for ZW-PCLG-3 of pneumatic pressure, resulting in a lattice form, which was deposited in a layer-by-layer fashion at a velocity of 170 mm/min. For *in vitro* study, the dimension of the ZW-PCLG scaffolds was 8×8 mm^2 with 2-mm thickness.

2.4. *In vitro* degradation test of ZW-PCLG scaffolds

The printed ZW-PCLG scaffolds ($8 \times 8 \times 2$ mm^3) were placed in 6-well plates containing 2 ml of PBS, and the plates were incubated on a shaker table (50 rpm) at 37°C for up to 8 weeks. For the NIR fluorescence imaging analysis, the ZW-PCLG scaffolds were washed twice with PBS and imaged, and the extracted media were also imaged in Eppendorf tubes using the 800-nm channel of Pearl® Impulse. The imaging data were collected and quantified by Pearl® Impulse software. The mean fluorescence was normalized by the initial NIR signal ($n = 6$ per group and time point).

To confirm the NIR imaging outcomes, the ZW-PCLG scaffolds were collected at the designated time points, freeze-dried, and weighed. The collected samples were dissolved in deuterated chloroform ($CDCl_3$) in the presence of tetramethylsilane (TMS) for proton nuclear magnetic resonance (^{1}H-NMR) analysis. The change in the molecular weight of ZW-PCLG copolymers under *in vitro* physiological condition was determined by comparing

the intensity of the proton signals in PCL, PLA, and PGA segments at ^{1}H-NMR peak (n = 3 per group and time point).

2.5. CTNF127 labeling to hPSCs (CT-PSCs)

The 700-nm NIR fluorescence emitting CTNF127 was synthesized as previously reported [34]. To optimize cell labeling, the hPSCs were cultured with different concentrations of CTNF127. Briefly, the cultured hPSCs were washed with PBS twice and incubated with 1–8 μM of CTNF127 (diluted in α-MEM without supplements) at 37°C. After 30–240 min, hPSCs were washed three times with PBS to remove unlabeled CTNF127. After 0, 3, and 5 days in culture, the cell viability and proliferation were analyzed by Live/Dead staining kit containing 2 mM calcein AM and 4 mM ethidium bromide (Life Technologies) and MTS assay kit (Abcam, Cambridge, UK), respectively. Live/dead cells were imaged using a fluorescence microscope (Zeiss Axio vert 200 M, Carl Zeiss, Oberkochen, Germany) and analyzed using an imaging analyzer (IN Cell Analyzer 1000, GE Healthcare, Waltham, MA, USA) (n = 5 per group and time point). For cell proliferation, the optical density (OD) was measured at 490 nm using a microplate reader (Spectra Max M5) (n = 6 per group and time point). To confirm the cell labeling, cellular NIR images were taken with a fluorescence microscope (Nikon, TE2000-U, Melville, NY) equipped with a 175 W full-spectrum Xenon lamp, QuantEM EMCCD camera (512SC, Photometrics, Tucson, AZ, USA), NIR-compatible optics (CY5.5 and CY7 Filter Set), and a NIR-compatible 10× Plan Fluor objective lens (Nikon) for NIR fluorescence analysis. Images were converted with white or pseudo color (red/green) and analyzed by InnerView™ (INNERVIEW Co., Sungnam, Korea). NIR fluorescence intensity from total cells in PBS was visualized by Pearl® Impulse (700-nm channel) and analyzed by Pearl® Impulse software (n = 6).

For printing process, the GelMA-based bioink that consists of 50 mg/ml GelMA, 3.75 mg/ml hyaluronic acid (HA), 12.5% (v/v) glycerol, 37.5 mg/ml of gelatin (Bloom 90–110), and 0.2% (w/v) Irgacure 2959 in α-MEM medium was used. The CT-PSCs were suspended in the GelMA-based bioink at 1×10^{6} cells/ml. This cell-laden GelMA bioink was loaded into a plastic syringe with a 300-μm Teflon nozzle and printed at 150 kPa of pneumatic pressure. After printing, the printed CT-PSC-laden constructs were crosslinked by UV light with a 320–500 nm filter (Exfo Omnicure S1000 lamp, Excelitas Technologies, Waltham, MA, USA) at a power density of 10 mW/cm^{2} at room temperature for 3 min. In order to evaluate the dye stability for cell tracking, the printed CT-PSC-laden constructs were printed based on the computer-aided design (CAD) design and placed in the CO_2 incubator for up to 20 days in culture. During the culture, the NIR images of the cell-laden constructs were taken using Pearl® Impulse for quantification (n = 6).

2.6. 3D printed CT-PSC-laden ZW-PCLG constructs for calvarial bone reconstruction

To validate the noninvasive *in vivo* monitoring of the scaffold degradation and stem cell tracking for bone regeneration in a rat calvarial bone defect model, the ZW-PCLG copolymers were printed together with the CT-PSC-laden GelMA-based bioink based on the printing conditions described above (ZW-PCLG-1 + CT-PSCs, ZW-PCLG-2 + CT-PSCs, and ZW-PCLG-3 + CT-PSCs). After printing, the upper and lower sides of the printed

constructs were crosslinked by UV as described above. For calvarial bone reconstruction, disk-shaped constructs of 7-mm diameter and 1-mm thickness were fabricated.

2.7. Rat calvarial bone defect model

All animal procedures were performed in accordance with a protocol (#A15–051) approved by the Institutional Animal Care and Use Committee (IACUC) at Wake Forest University Health Sciences. The calvarial bone defect model was created in Sprague Dawley rats (male, 8 weeks old, Charles River Laboratories Inc., Wilmington, MA). Under the general anesthesia, the top of the cranium was exposed by a midline incision of skin and periosteum. A cooled stainless-steel trephine burr (7-mm diameter) and a surgical drill were used to create a 7-mm diameter calvarial bony defect. After the printed CT-PSC-laden ZW-PCLG construct was implanted into the defect, the incision was closed with a 5–0 absorbable suture for periosteum and 4–0 non-absorbable suture for the skin. The cutaneous suture was removed 7–10 days after implantation. Animals were monitored weekly for 8 weeks using the Pearl® Impulse system. Six experimental groups were conducted (n = 3 per group and per time point, total 72 animals); (1) ZW-PCLG-1, (2) ZW-PCLG-2, (3) ZW-PCLG-3, (4) ZW-PCLG-1 + CT-PSCs, (5) ZW-PCLG-2 + CT-PSCs and (6) ZW-PCLG-3 + CT-PSCs.

2.8. *In vivo* NIR fluorescence imaging

To noninvasively monitor the scaffold degradation, animals were anesthetized, and NIR images of the implanted constructs were taken weekly using *in vivo* imaging system (Pearl® Impulse) quipped with a 700-nm channel (excitation 685 nm, emission 720 nm), 800-nm channel (excitation 785 nm, emission 820 nm), and white channel (excitation white, emission NA). Imaging data were collected and quantified by Impulse software (Pearl® Software Images, LICOR). The region of interest (ROI) was the whole area where the signal was expressed over the implanted construct. The mean of the fluorescence intensity (FL mean; arbitrary unit) or the value normalized by the initial intensity was presented in the results (n = 6 per group and time point).

2.9. Computed tomography (CT) analysis

CT scan was carried out to examine new bone formation in the calvarial bone defected region. Animals were kept under general anesthesia during the procedure. The skull bone was imaged using a Toshiba 32-Slice Aquilion computed tomography (CT) scanner (Providian Medical Equipment LLC. Highland Heights, OH), which has the capability of imaging 0.5 mm-thick tissue slices. The scanned images were then processed with Mimics version 13 (Materialise, Leuven, Belgium), which provides 3D viewing capabilities.

2.10. Scanning electron microscopy (SEM) observation

The retrieved constructs were observed using SEM (S-2250N, Hitachi, Japan). Samples were coated with platinum for 30 sec under an argon atmosphere, using a plasma sputter coater (SC 500K, Emscope, UK). The images were acquired at an accelerating voltage of 25 kV with a 15-cm working distance.

2.11. Molecular weight measurement

At the designed time points, the implanted constructs were retrieved and lyophilized. For gel permeation chromatography (GPC) and ^{1}H NMR, the lyophilized samples were dissolved in dichloromethane (CH_2Cl_2) to extract the PCLG copolymers. After the addition of deionized water, the resulting solution was sonicated at 25°C for 90 min. The CH_2Cl_2 phase was separated from the solution and evaporated. The extracted PCLG copolymers were dissolved in chloroform ($CHCl_3$) for GPC and deuterated chloroform ($CDCl_3$) for ^{1}H NMR ($n = 3$ per group and time point).

2.12. Histological analysis and NIR cell tracking

The retrieved constructs were fixed for 48 h in 10% neutral-buffered formalin, then decalcified in Richard Allan Scientific Decalcifying Solution (Thermo Scientific) for 24 h. The samples were rinsed with DI water, dipped in 30% sucrose for 24 h, and cryo-embedded in liquid nitrogen for sectioning. The samples were cryosectioned (10-μm thick) and analyzed by hematoxylin and eosin (H&E) and modified Tetrachrome staining. For NIR imaging, the cryosectioned samples were observed under 700-nm and 800-nm NIR fluorescence, respectively. The samples were treated with DAPI staining to visualize nuclei.

2.13. Statistical analysis

Data were analyzed with Student's *t*-test or one-way ANOVA using GraphPad Prism software (GraphPad Software, Inc., La Jolla, CA). $P < 0.05$ was considered statistically significant.

3. Results and discussion

3.1. Synthesis of NIR-functionalized copolymers with different degradation rates

The scaffold degradability has been considered to be a critical parameter that directly related to successful tissue regeneration [35–38]. It has also been reported that the metabolic activity of the transplanted cells in the scaffold is influenced by scaffold degradation [36]. Biodegradable polyesters such as polylactide (PLA), polyglycolide (PGA), poly(lactide-*co*-glycolide) (PLGA), and poly(ε-caprolactone) (PCL) are the most commonly used as scaffold materials for tissue engineering applications. We previously incorporated poly(L-lactic acid) (PLLA) segment into the PCL to improve the water accessibility of PCL-based scaffolds, resulting in accelerated degradation by hydrolysis [39–41]. This PLLA-ran-PCL copolymer was capable of controlled release of growth factors or drugs based on the ratios of LA and CL. In this study, we designed and synthesized three PCL-ran-PCL-Cl-ran-PLLA-ran-PGA copolymers, PCLG1-Cl, PCLG2-Cl, and PCLG3-Cl, by using different monomer ratios to control the scaffold degradation (Table 1 and Fig. 2A). The molecular weights and monomer ratios of each copolymer were calculated from the ^{1}H-NMR data by comparison with MPEG as a standard (Fig. 2B). The calculated monomer ratios of the copolymers (PCLG-1, PCLG-2, and PCLG-3) agreed well with the expected values. The contents of α-chloro-ε-caprolactone (CL-Cl) were detected by ^{13}C-NMR spectra through the comparing carbonyl signal of CL-Cl at δ = 167 ppm with that of PLLA at δ = 169 ppm. The chlorines in the synthesized copolymers (PCLGs-Cl) were displaced with azide for the introduction of amine

via the reduction of the azide group. The introduced azide groups are detected with FT-IR at a wavenumber of approximately 2100 cm^{-1} (Fig. 2C).

NH_2-functionalized PCLG copolymers were obtained by reducing of PCLGs-N_3 using PPh_3. We determined the disappearance of azide peaks in the spectra by the reduction in signal intensity at 2100 cm^{-1}. To introduce the NIR fluorophore in the PCLG copolymers, we used chloro-caprolactone (CL-Cl) as a monomer. The Cl is substituted to the azide group via nucleophilic substitution, and the azide group is reduced to the amine or changed to other functional groups. The NH_2-functionalized PCLG copolymers could be utilized to conjugate bioactive molecules such as small molecules, drugs, peptides, growth factors, and genes.

For NIR fluorescence imaging, 800-nm emitting ZW800–1C was conjugated on the PCLG copolymers (ZW-PCLGs). The *N*-hydroxysuccinimide (NHS)-activated ZW800–1C ester was reacted with the NH_2-functionalized PCLG copolymers (Fig. 2D). It has previously been reported that the ZW800–1C fluorophore has stable physicochemical and optical properties against enzymes and shows no cytotoxicity in mice, rats, and pigs [22]. Furthermore, this NIR fluorophore has minimum serum protein binding, low nonspecific tissue uptake, and rapid elimination from the body [42, 43]. In addition, we selected two NIR fluorophores, ZW800–1C (800 nm) and CTNF127 (700 nm), for this present study because there is no detectable overlap between fluorophores (Supplementary Fig. S1).

3.2. Evaluation of *in vitro* scaffold degradation

It is generally accepted that the structural parameters such as porosity and pore size and morphology can influence the scaffold degradation behavior [44]. In order to avoid the effect of these structural parameters, we used 3D bioprinting technology to fabricate the ZW-PCLG-based scaffolds based on the CAD design (Fig. 3A). In this study, we utilized our ITOP system that could fabricate stable, human-scale tissue constructs through multiple dispensing of cell-laden hydrogels together with supporting polymeric materials [2]. To confirm the thermal stability of the PCLG copolymers during the 3D printing process, we analyzed the change in the molecular weight of the PCLG copolymers at 100°C. The PCLG-2 copolymer was able to maintain its thermal stability based on the molecular weight at 100°C for up to 6 h (Supplementary Fig. S2). After printing, the ZW-PCLG scaffolds were green in color, which is the intrinsic color of ZW800–1C. The 800-nm fluorescence emitted by the ZW-PCLG scaffolds was expressed in green pseudo color by the dual channel imaging system. 3D printed ZW-PCLG scaffolds presented well-regulated and uniform pores with a spacing of 150 μm between the printed strands.

To optimize the NIR fluorophore conjugation to detect the NIR signal from the ZW-PCLG scaffolds, various molar ratios (0.01, 0.05, 0.1, 0.5, and 2.0) of ZW800–1C:PCLG-NH_2 copolymer were tested. The *in vitro* degradation of the printed ZW-PCLG scaffolds with different molar ratios of ZW-800–1Cwas determined by measuring the NIR fluorescence signals from the scaffolds in PBS at 37°C for up to 30 days (Fig. 3B). The NIR signal from the ZW-PCLG scaffold decreased gradually with ZW800–1C:PCLG-NH_2 ratios of 0.01, 0.05, 0.1, and 0.5 (Fig. 3C). In contrast, the scaffolds with a ratio of 2.0 showed a continuous increase in NIR signal with time due to the aggregation caused quenching at the initial time point. Based on this result, we selected the molar ratio of 0.5 for further experiments because

this molar ratio in the ZW-PCLG scaffolds showed the highest fluorescence intensity with the minimum quenching phenomenon.

To investigate whether the NIR imaging could measure the degradation rate of polymeric materials under the *in vitro* physiological condition, we monitored the NIR fluorescence signals of the printed ZW-PCLG scaffolds (ZW-PCLG-1, ZW-PCLG-2, and ZW-PCLG-3) for up to 8 weeks of incubation (Fig. 3D). Based on the NIR imaging quantification, a gradual reduction of fluorescence intensity in the printed scaffolds was observed over time (Fig. 3E), while an accumulated signal increased gradually in the incubation buffer (Fig. 3F). For comparison, we also measured the molecular weights of PCLG copolymers using ^{1}H NMR (Fig. 3G) and the mass reduction by weighing (Fig. 3H). At 8 weeks of incubation, the remained NIR signals from the printed scaffolds were 32.8% for ZW-PCLG-1, 33.7% for ZW-PCLG-2, and 87% for ZW-PCLG-3. Similarly, the molecular weights maintained were 52.2% for ZW-PCLG-1, 53.3% for ZW-PCLG-2, and 94.0% for ZW-PCLG-3 as measured by ^{1}H NMR, and mass remained were 51.5% for ZW-PCLG-1, 64.5% for ZW-PCLG-2, and 91.5% for ZW-PCLG-3. These results indicated that the PCLG copolymers were successfully synthesized with different degradation behaviors and conjugated with the NIR fluorophore for further *in vivo* imaging analysis to determine scaffold degradation. The synthesized PCLG copolymers could be degraded by, mainly, hydrolysis of their ester linkages. The PCLG-3 copolymer was designed to be more hydrophobic compared with PCLG-1 and PCLG-2, resulting in relatively slow degradation behavior.

3.3. *In vitro* evaluation of CTNF127-labeled hPSCs

Stem cell-based tissue engineering requires *in vitro* expansion of stem cells with high proliferative and osteogenic potentials to support new bone tissue formation. In this study, we used human placental stem cells (hPSCs) as a cell source. These cells obtained with high yield from placentas discarded after childbirth can be expanded quickly *in vitro* and have a remarkable ability to differentiate into multiple cell types, encompassing the three germ layers, and to sustain undifferentiated proliferation for a prolonged time [45, 46]. Furthermore, it has been reported that hPSCs could facilitate the repair of bone defects by secreting osteogenically-active factors [47, 48]. To evaluate the osteogenic differentiation capacity of hPSCs, the cells were cultured under the osteogenic medium condition for up to 40 days. The results strongly supported the osteogenic differentiation capacity of hPSCs as confirmed by Alizarin Red S and alkaline phosphatase (ALP) staining assay and von Kossa staining (Supplementary Fig. S3).

To optimize the NIR labeling for cell tracking, 1–8 μM of CTNF127 fluorophores were tested in hPSCs. Since CTNF fluorophores are lysosome-fixable cell tracking NIR fluorophores with presenting enhanced cell permeation and retention, as well as high stability in the biological condition, CTNF127 can efficiently track the host cells during tissue regeneration [34]. Moreover, CTNF127 is composed of the polymethine backbone, which is inherently nontoxic and biocompatible based on the decades-long clinical evaluation of the FDA-approved fluorophore indocyanine green [34]. The lipophilic polymethine core of CTNF127 allows passive diffusion across cell membranes and the protonated primary amine holds the fluorophore inside the lysosome via ion trapping at a

lower pH, preventing to reach the nucleus and enabling longitudinal monitoring of the transplanted cells. Live/Dead staining assay revealed that cell viability (%) decreased at the concentrations of 4 and 8 μM of CTNF127 at early time points, which was recovered after 3 days in culture (*P<0.05, Fig. 4A,B). An overall increase in the proliferation of hPSCs was observed over the incubation time; however, 8 μM of CTNF127 reduced cellular density compared to others (*P<0.05, Fig. 4C). In addition, 700-nm NIR fluorescence signals were saturated and quenched in the cells incubated with 4 μM of CTNF127 (Fig. 4D,E). Based on these results, to avoid aggregation caused by quenching and cytotoxicity, 2 μM of CTNF127 was selected for labeling hPSCs (CT-PSCs) for further experiments.

To detect the 700-nm NIR fluorescence signal from the CT-PSCs (treated with 2 μM of CTNF127) in the 3D printed hydrogel constructs, the cells were printed with a gelatin methacrylate (GelMA)-based bioink according to the CAD design (Fig. 4F). The GelMA was characterized by ^{1}H NMR before the use (Supplementary Fig. S4). The printed CT-PSC-laden constructs had sequential increasing layer number from 1 to 6. The NIR fluorescence intensity increased proportionally with the number of printed layers (Fig. 4G). More importantly, the NIR fluorescence signal in the printed CT-PSC-laden constructs was maintained approximately 76% during 20 days in culture (Fig. 4H). The results indicated that CTNF127 fluorophore offered a strong NIR fluorescence signal after cell labeling with minimum cytotoxic effects. Moreover, the continued fluorescent emission of CT-PSCs within the hydrogel-based 3D construct could be suitable for evaluating the stem cell fate *in vivo*. In addition, we confirmed the stability of both ZW800–1C and CTNF127 under UV exposure since the photocrosslinking was required to improve the GelMA-based hydrogel constructs after 3D printing. The results showed the UV exposure did not disturb the fluorescent intensity of both fluorophores (Supplementary Fig. 5S).

3.4. Quantitative real-time monitoring of *in vivo* degradation of ZW-PCLG scaffolds

For *in vivo* validation, a hybrid construct of the CT-PSC-laden hydrogel and the ZW-PCLG scaffold was fabricated by the ITOP system using the parameters determined in the previous sections. Fluorescence signals were completely distinguished from CT-PSCs at 700-nm wavelength and ZW-PCLG copolymers at 800-nm wavelength (Fig. 5A). After construct implantation, the degradation behavior of ZW-PCLG-based scaffolds was noninvasively monitored based on 800-nm fluorescence signal for up to 8 weeks (Fig. 5B). Our NIR imaging system provided a clear fluorescence signal under the skin because the NIR beam could penetrate the periosteum (0.1 mm) [49] and skin (1.2 mm) [50].The quantified NIR fluorescence signals at 800 nm obtained from the implanted PCLG scaffolds presented a constant reduction over time, indicating the scaffold degradation (Fig. 5D). The rate of signal reduction was notably faster in the ZW-PCLG-1 and ZW-PCLG-2 scaffolds; however, the ZW-PCLG scaffolds retained over 50% fluorescence signal at 8 weeks of implantation.

To visualize the scaffold degradation, the ultrastructure of the retrieved PCLG scaffolds were observed by SEM (Fig. 5C). The results revealed that the printed ZW-PCLG-1 scaffold was rapidly degraded and completely collapsed at 8 weeks of implantation. The printed ZW-PCLG-3 showed the structural integrity at 8 weeks of implantation, indicating the slow degradation behavior. To confirm these outcomes, change in the molecular weight was

measured by GPC (Fig. 5E) and ^{1}H NMR (Fig. 5F and Supplementary Fig. S6). These results showed a similar tendency in comparison with the NIR-based noninvasive monitoring for the *in vivo* scaffold degradation.

Together, molecular imaging can combine or replace traditional methods of scaffold degradation such as molecular weight, macro- or micromorphology, mass loss, and histological examination, which can minimize the use of numerous samples and animals at various time points [22].

3.5. *In vivo* evaluation of stem cell-mediated bone regeneration

New bone formation in the defected calvarial bone was assessed by CT after 8 weeks of implantation (Fig. 6A). The CT analysis indicated that the printed ZW-PCLG-3 constructs both with and without CT-PSCs showed the highest new bone formation compared with others. In the histological examination, the modified Tetrachrome staining confirmed mature bone (red) and osteoid (blue) formation (Fig. 6B). The printed ZW-PCLG-3 constructs with CT-PSCs showed newly formed bone tissue in the implanted constructs, whereas the ZW-PCLG-1 construct both with and without CT-PSCs showed fibrotic tissue ingrowth with no evidence of new bone formation. In addition, the printed ZW-PCLG-3 constructs without cells showed minimal bone tissue formation restricted to the periphery of the constructs.

To determine the stem cell-mediated bone regeneration along with scaffold degradation, the histological sections were observed throughout the NIR fluorescence; 700 nm for CT-PSCs and 800 nm for ZW-PCLGs (Fig. 6C). The histological outcomes showed that the slow degradable ZW-PCLG-3 scaffolds maintained the structural integrity at 8 weeks of implantation, and the ZW-PCLG-3 + CT-PSCs constructs allowed the highest new bone formation, indicating that both stem cells together with the scaffold degradation behavior could contribute in bone tissue regeneration. Particularly, we could still observe the existence of the transplanted hPSCs in the newly formed bone by NIR fluorescent images (Fig. 6D), which supported the direct differentiation of hPSCs into the osteogenic cells. In contrast, the printed ZW-PCLG-1 scaffolds were rapidly degraded at 4 and 8 weeks after implantation, resulting in the structural collapse that did not allow the new bone formation. Even though new bone formation was enhanced by the hPSCs in the ZW-PCLG-3 scaffolds, the ZW-PCLG-1 scaffolds with hPSCs did not show any newly formed bone. This was also confirmed by fluorescent images with the same sections; weaker and more dispersed green and red pseudo colors were detected in the ZW-PCLG-1 groups. In the ZW-PCLG-2 groups, there was no evidence for new bone formation both with and without hPSCs. Even though the ZW-PCLG-2 scaffolds maintained partial structural integrity, the porous structure seemed to be tightened, resulting in the minimum cellular infiltration and fibrous tissue formation. The results revealed that only slowly degradable PCLG-3 scaffolds could induce new bone formation, and hPSCs could improve the newly formed bone only in the PCLG-3 scaffolds. Our findings in this study could suggest that maintaining the porous structure in the scaffold during neo-tissue formation could be crucial for successful reconstruction. Additionally, it has been reported that the byproducts during the degradation of the polymer network could not elicit a negative cellular response [51].

Although NIR fluorescence imaging offers great potential for noninvasive monitoring of tissue regeneration, the limited penetration depth is a major limitation in reflectance-based fluorescence imaging. Recent advances in imaging systems including fluorescence tomography, fluorescence lifetime imaging, and photoacoustic imaging [52, 53] can further improve the imaging depth, while the use of NIR-II window (1,000–1,700 nm) can maximize the fluorescence signal intensity by reducing photon scattering in the neighboring tissues [54, 55]. Otherwise, multimodal imaging combining NIR imaging with other imaging modalities such as MRI, mesoscale imaging, and microCT could be useful to improve the spatial resolution of soft/hard tissues in regenerative medicine [56, 57]. For instance, chemical exchange saturation transfer (CEST) MRI has been utilized for monitoring the degradation of a gelatin-based hydrogel system [58, 59].

4. Conclusions

We successfully synthesized the NH_2-functionalized PCL-*ran*-PLLA-*ran*-PGA (PCLG) copolymers using different ratios of CL, LA, and GA monomers. These PCLG copolymers were designed to acquire different degradation rates by controlling the monomer ratios. Moreover, we were able to introduce the NIR fluorophore (ZW800–1C, 800 nm) on the PCLG copolymers by chemical conjugation for noninvasive monitoring of the 3D printed PCLG-based scaffolds. In addition, we successfully utilized the 700 nm NIR channel by labeling CTNF127 in the hPSCs for histological analysis. To investigate the effects of the scaffold degradation along with the transplanted stem cells for bone tissue regeneration, we fabricated the 3D tissue constructs by co-printing the CT-PSC-laden GelMA-based bioink with the ZW-PCLGs and implanted in the rat calvarial bone defect model. The results strongly suggested the NIR imaging could noninvasively monitor the degradation behaviors of the 3D printed ZW-PCLG-based scaffolds *in vivo*. We demonstrated that the slowly degradable PCLG scaffold with hPSCs showed the highest new bone formation compared to the rapid degradable PCLG scaffolds as confirmed by the NIR-based noninvasive monitoring of the scaffold degradation along with stem cell tracking. This system could provide a better understanding of the regenerative mechanism using the stem cells, as well as a scaffold design strategy for tissue engineering applications.

Supplementary Material

Refer to Web version on PubMed Central for supplementary material.

Acknowledgments

This study was supported by the following NIH grants: #P41EB023833, #R01EB022230, and #R01HL143020. This work was also supported by the Creative Materials Discovery Program (2019M3D1A1078938) and Priority Research Centers Program (2019R1A6A1A11051471) through the National Research Foundation of Korea (NRF).

References

[1]. Atala A, Kasper FK, Mikos AG, Engineering complex tissues, Sci Transl Med 4(160) (2012) 160rv12.

[2]. Kang H-W, Lee SJ, Ko IK, Kengla C, Yoo JJ, Atala A, A 3D bioprinting system to produce human-scale tissue constructs with structural integrity, Nature biotechnology 34(3) (2016) 312–319.

[3]. Hutmacher DW, Scaffolds in tissue engineering bone and cartilage, Biomaterials 21(24) (2000) 2529–43. [PubMed: 11071603]

[4]. Middleton JC, Tipton AJ, Synthetic biodegradable polymers as orthopedic devices, Biomaterials 21(23) (2000) 2335–46. [PubMed: 11055281]

[5]. Salazar-Noratto GE, Luo G, Denoeud C, Padrona M, Moya A, Bensidhoum M, Bizios R, Potier E, Logeart-Avramoglou D, Petite H, Understanding and leveraging cell metabolism to enhance mesenchymal stem cell transplantation survival in tissue engineering and regenerative medicine applications, Stem Cells 38(1) (2020) 22–33. [PubMed: 31408238]

[6]. Brassard JA, Lutolf MP, Engineering Stem Cell Self-organization to Build Better Organoids, Cell Stem Cell 24(6) (2019) 860–876. [PubMed: 31173716]

[7]. Loebel C, Burdick JA, Engineering Stem and Stromal Cell Therapies for Musculoskeletal Tissue Repair, Cell Stem Cell 22(3) (2018) 325–339. [PubMed: 29429944]

[8]. da Rocha DN, Marçal RLSB, Barbosa RM, Ferreira JRM, da Silva MHP, Mesenchymal Stem Cells Associated with Bioceramics for Bone Tissue Regeneration, Biomaterials and Medical Applications 2017 (2018).

[9]. Kim C-H, Lim C-Y, Lee J-H, Kim KC, Ahn JY, Lee EJ, Human Embryonic Stem Cells-Derived Mesenchymal Stem Cells Reduce the Symptom of Psoriasis in Imiquimod-Induced Skin Model, Tissue engineering and regenerative medicine 16(1) (2019) 93–102. [PubMed: 30815354]

[10]. Shahmoradi SR, Salmani MK, Soleimanpour HR, Tavakoli AH, Hosaini K, Haghighipour N, Bonakdar S, Induction of Chondrogenic Differentiation in Human Mesenchymal Stem Cells Cultured on Human Demineralized Bone Matrix Scaffold under Hydrostatic Pressure, Tissue engineering and regenerative medicine 16(1) (2019) 69–80. [PubMed: 30815352]

[11]. Meir R, Shamalov K, Betzer O, Motiei M, Horovitz-Fried M, Yehuda R, Popovtzer A, Popovtzer R, Cohen CJ, Nanomedicine for Cancer Immunotherapy: Tracking Cancer-Specific T-Cells in Vivo with Gold Nanoparticles and CT Imaging, ACS Nano 9(6) (2015) 6363–72. [PubMed: 26039633]

[12]. Finamore TA, Curtis TE, Tedesco JV, Grandfield K, Roeder RK, Nondestructive, longitudinal measurement of collagen scaffold degradation using computed tomography and gold nanoparticles, Nanoscale 11(10) (2019) 4345–4354. [PubMed: 30793721]

[13]. Vila OF, Martino MM, Nebuloni L, Kuhn G, Pérez-Amodio S, Müller R, Hubbell JA, Rubio N, Blanco J, Bioluminescent and micro-computed tomography imaging of bone repair induced by fibrin-binding growth factors, Acta biomaterialia 10(10) (2014) 4377–4389. [PubMed: 24905933]

[14]. Arbab AS, Yocum GT, Kalish H, Jordan EK, Anderson SA, Khakoo AY, Read EJ, Frank JA, Efficient magnetic cell labeling with protamine sulfate complexed to ferumoxides for cellular MRI, Blood 104(4) (2004) 1217–1223. [PubMed: 15100158]

[15]. Lalande C, Miraux S, Derkaoui S, Mornet S, Bareille R, Fricain J-C, Franconi J-M, Le Visage C, Letourneur D, Amédée J, Magnetic resonance imaging tracking of human adipose derived stromal cells within three-dimensional scaffolds for bone tissue engineering, Eur Cell Mater 21(1) (2011) 341–354. [PubMed: 21484704]

[16]. Yang JJ, Liu ZQ, Zhang JM, Wang HB, Hu SY, Liu JF, Wang CY, Chen YD, Real-time tracking of adipose tissue-derived stem cells with injectable scaffolds in the infarcted heart, Heart Vessels 28(3) (2013) 385–96. [PubMed: 22940832]

[17]. Souron JB, Petiet A, Decup F, Tran XV, Lesieur J, Poliard A, Le Guludec D, Letourneur D, Chaussain C, Rouzet F, Opsahl Vital S, Pulp cell tracking by radionuclide imaging for dental tissue engineering, Tissue Eng Part C Methods 20(3) (2014) 188–97. [PubMed: 23789732]

[18]. Wolbank S, Pichler V, Ferguson JC, Meinl A, van Griensven M, Goppelt A, Redl H, Non-invasive in vivo tracking of fibrin degradation by fluorescence imaging, J Tissue Eng Regen Med 9(8) (2015) 973–6. [PubMed: 25044309]

[19]. Artzi N, Oliva N, Puron C, Shitreet S, Artzi S, bon Ramos A, Groothuis A, Sahagian G, Edelman ER, In vivo and in vitro tracking of erosion in biodegradable materials using non-invasive fluorescence imaging, Nat Mater 10(9) (2011) 704–9. [PubMed: 21857678]

[20]. Wang W, Liu J, Li C, Zhang J, Liu J, Dong A, Kong D, Real-time and non-invasive fluorescence tracking of in vivo degradation of the thermosensitive PEGlyated polyester hydrogel, Journal of Materials Chemistry B 2(26) (2014) 4185–4192. [PubMed: 32261752]

[21]. Nakayama A, del Monte F, Hajjar RJ, Frangioni JV, Functional near-infrared fluorescence imaging for cardiac surgery and targeted gene therapy, Mol Imaging 1(4) (2002) 365–77. [PubMed: 12940233]

[22]. Kim SH, Lee JH, Hyun H, Ashitate Y, Park G, Robichaud K, Lunsford E, Lee SJ, Khang G, Choi HS, Near-infrared fluorescence imaging for noninvasive trafficking of scaffold degradation, Scientific reports 3 (2013).

[23]. Owens EA, Henary M, El Fakhri G, Choi HS, Tissue-Specific Near-Infrared Fluorescence Imaging, Acc Chem Res 49(9) (2016) 1731–40. [PubMed: 27564418]

[24]. Miao Q, Xie C, Zhen X, Lyu Y, Duan H, Liu X, Jokerst JV, Pu K, Molecular afterglow imaging with bright, biodegradable polymer nanoparticles, Nat Biotechnol 35(11) (2017) 1102–1110. [PubMed: 29035373]

[25]. Huang J, Li J, Lyu Y, Miao Q, Pu K, Molecular optical imaging probes for early diagnosis of drug-induced acute kidney injury, Nat Mater 18(10) (2019) 1133–1143. [PubMed: 31133729]

[26]. Gioux S, Choi HS, Frangioni JV, Image-guided surgery using invisible near-infrared light: fundamentals of clinical translation, Mol Imaging 9(5) (2010) 237–55. [PubMed: 20868625]

[27]. Owens EA, Lee S, Choi J, Henary M, Choi HS, NIR fluorescent small molecules for intraoperative imaging, Wiley Interdiscip Rev Nanomed Nanobiotechnol 7(6) (2015) 828–38. [PubMed: 25645081]

[28]. Choi HS, Frangioni JV, Nanoparticles for biomedical imaging: fundamentals of clinical translation, Mol Imaging 9(6) (2010) 291–310. [PubMed: 21084027]

[29]. Park JH, Lee BK, Park SH, Kim MG, Lee JW, Lee HY, Lee HB, Kim JH, Kim MS, Preparation of Biodegradable and Elastic Poly (ε-caprolactone-co-lactide) Copolymers and Evaluation as a Localized and Sustained Drug Delivery Carrier, International journal of molecular sciences 18(3) (2017) 671.

[30]. Hyun H, Owens EA, Narayana L, Wada H, Gravier J, Bao K, Frangioni JV, Choi HS, Henary M, Central C–C bonding increases optical and chemical stability of NIR fluorophores, RSC advances 4(102) (2014) 58762–58768. [PubMed: 25530846]

[31]. Kim KS, Hyun H, Yang J-A, Lee MY, Kim H, Yun S-H, Choi HS, Hahn SK, Bioimaging of Hyaluronate–Interferon α Conjugates Using a Non-Interfering Zwitterionic Fluorophore, Biomacromolecules 16(9) (2015) 3054–3061. [PubMed: 26258264]

[32]. Choi HS, Nasr K, Alyabyev S, Feith D, Lee JH, Kim SH, Ashitate Y, Hyun H, Patonay G, Strekowski L, Synthesis and In Vivo Fate of Zwitterionic Near-Infrared Fluorophores, Angewandte Chemie International Edition 50(28) (2011) 6258–6263. [PubMed: 21656624]

[33]. Merceron TK, Burt M, Seol Y-J, Kang H-W, Lee SJ, Yoo JJ, Atala A, A 3D bioprinted complex structure for engineering the muscle–tendon unit, Biofabrication 7(3) (2015) 035003. [PubMed: 26081669]

[34]. Park GK, Lee JH, Levitz A, El Fakhri G, Hwang NS, Henary M, Choi HS, Lysosome-Targeted Bioprobes for Sequential Cell Tracking from Macroscopic to Microscopic Scales, Advanced Materials 31(14) (2019) 1806216.

[35]. Bryant SJ, Anseth KS, Hydrogel properties influence ECM production by chondrocytes photoencapsulated in poly (ethylene glycol) hydrogels, Journal of Biomedical Materials Research: An Official Journal of The Society for Biomaterials and The Japanese Society for Biomaterials 59(1) (2002) 63–72.

[36]. Alsberg E, Kong H, Hirano Y, Smith M, Albeiruti A, Mooney D, Regulating bone formation via controlled scaffold degradation, Journal of dental research 82(11) (2003) 903–908. [PubMed: 14578503]

[37]. Sung H-J, Meredith C, Johnson C, Galis ZS, The effect of scaffold degradation rate on three-dimensional cell growth and angiogenesis, Biomaterials 25(26) (2004) 5735–5742. [PubMed: 15147819]

[38]. Depan D, Shah J, Misra R, Degradation mechanism and increased stability of chitosan-based hybrid scaffolds cross-linked with nanostructured carbon: Process–structure–functional property relationship, Polymer degradation and Stability 98(11) (2013) 2331–2339.

[39]. Choi JW, Kim YS, Park JK, Song EH, Park JH, Kim MS, Shin YS, Kim CH, Controlled Release of Hepatocyte Growth Factor from MPEG-b-(PCL-ran-PLLA) Diblock Copolymer for Improved Vocal Fold Regeneration, Macromolecular bioscience 17(2) (2017) 1600163.

[40]. Seo HW, Kwon DY, Kwon JS, Jin LM, Lee B, Kim JH, Min BH, Kim MS, Injectable intratumoral hydrogel as 5-fluorouracil drug depot, Biomaterials 34(11) (2013) 2748–2757. [PubMed: 23343635]

[41]. Kang YM, Lee SH, Lee JY, Son JS, Kim BS, Lee B, Chun HJ, Min BH, Kim JH, Kim MS, A biodegradable, injectable, gel system based on MPEG-b-(PCL-ran-PLLA) diblock copolymers with an adjustable therapeutic window, Biomaterials 31(9) (2010) 2453–2460. [PubMed: 20022371]

[42]. Choi HS, Gibbs SL, Lee JH, Kim SH, Ashitate Y, Liu F, Hyun H, Park G, Xie Y, Bae S, Targeted zwitterionic near-infrared fluorophores for improved optical imaging, Nature biotechnology 31(2) (2013) 148–153.

[43]. Hyun H, Bordo MW, Nasr K, Feith D, Lee JH, Kim SH, Ashitate Y, Moffitt LA, Rosenberg M, Henary M, cGMP-Compatible preparative scale synthesis of near-infrared fluorophores, Contrast media & molecular imaging 7(6) (2012) 516–524. [PubMed: 22991318]

[44]. Eglin D, Mortisen D, Alini M, Degradation of synthetic polymeric scaffolds for bone and cartilage tissue repairs, Soft Matter 5(5) (2009) 938–947.

[45]. Delo DM, De Coppi P, Bartsch G Jr, Atala A, Amniotic fluid and placental stem cells, Methods in enzymology, Elsevier2006, pp. 426–438. [PubMed: 17141065]

[46]. Murphy SV, Atala A, Amniotic fluid and placental membranes: unexpected sources of highly multipotent cells, Seminars in reproductive medicine, Thieme Medical Publishers, 2013, pp. 062–068.

[47]. Cheng C-C, Chung C-A, Su L-C, Chien C-C, Cheng Y-C, Osteogenic differentiation of placenta-derived multipotent cells in vitro, Taiwanese Journal of Obstetrics and Gynecology 53(2) (2014) 187–192. [PubMed: 25017264]

[48]. Zhong ZN, Zhu SF, Yuan AD, Lu GH, He ZY, Fa ZQ, Li WH, Potential of placenta-derived mesenchymal stem cells as seed cells for bone tissue engineering: preliminary study of osteoblastic differentiation and immunogenicity, Orthopedics 35(9) (2012) 779–788. [PubMed: 22955387]

[49]. Moore SR, Milz S, Knothe Tate ML, Periosteal thickness and cellularity in mid-diaphyseal cross-sections from human femora and tibiae of aged donors, Journal of anatomy 224(2) (2014) 142–149. [PubMed: 24175932]

[50]. Takeuchi H, Ishida M, Furuya A, Todo H, Urano H, Sugibayashi K, Influence of skin thickness on the in vitro permeabilities of drugs through Sprague-Dawley rat or Yucatan micropig skin, Biological and Pharmaceutical Bulletin 35(2) (2012) 192–202. [PubMed: 22293349]

[51]. Wang MO, Piard CM, Melchiorri A, Dreher ML, Fisher JP, Evaluating changes in structure and cytotoxicity during in vitro degradation of three-dimensional printed scaffolds, Tissue Eng Part A 21(9–10) (2015) 1642–53. [PubMed: 25627168]

[52]. Jiang Y, Upputuri PK, Xie C, Zeng Z, Sharma A, Zhen X, Li J, Huang J, Pramanik M, Pu K, Metabolizable Semiconducting Polymer Nanoparticles for Second Near-Infrared Photoacoustic Imaging, Adv Mater 31(11) (2019) e1808166. [PubMed: 30663820]

[53]. Jiang Y, Pu K, Molecular fluorescence and photoacoustic imaging in the second near- infrared optical window using organic contrast agents, Advanced Biosystems 2(5) (2018) 1700262.

[54]. Son J, Yi G, Yoo J, Park C, Koo H, Choi HS, Light-responsive nanomedicine for biophotonic imaging and targeted therapy, Adv Drug Deliv Rev 138 (2019) 133–147. [PubMed: 30321619]

[55]. Park GK, Kim SH, Kim K, Das P, Kim BG, Kashiwagi S, Choi HS, Hwang NS, Dual-Channel Fluorescence Imaging of Hydrogel Degradation and Tissue Regeneration in the Brain, Theranostics 9(15) (2019) 4255–4264. [PubMed: 31285760]

[56]. Kang H, Hu S, Cho MH, Hong SH, Choi Y, Choi HS, Theranostic Nanosystems for Targeted Cancer Therapy, Nano Today 23 (2018) 59–72. [PubMed: 31186672]

[57]. Sajedi S, Sabet H, Choi HS, Intraoperative biophotonic imaging systems for image-guided interventions, Nanophotonics 8(1) (2019) 99–116. [PubMed: 31187017]

[58]. Zhu W, Chu C, Kuddannaya S, Yuan Y, Walczak P, Singh A, Song X, Bulte JWM, In Vivo Imaging of Composite Hydrogel Scaffold Degradation Using CEST MRI and Two-Color NIR Imaging, Adv Funct Mater 29(36) (2019).

[59]. Liang Y, Bar-Shir A, Song X, Gilad AA, Walczak P, Bulte JW, Label-free imaging of gelatin-containing hydrogel scaffolds, Biomaterials 42 (2015) 144–50. [PubMed: 25542802]

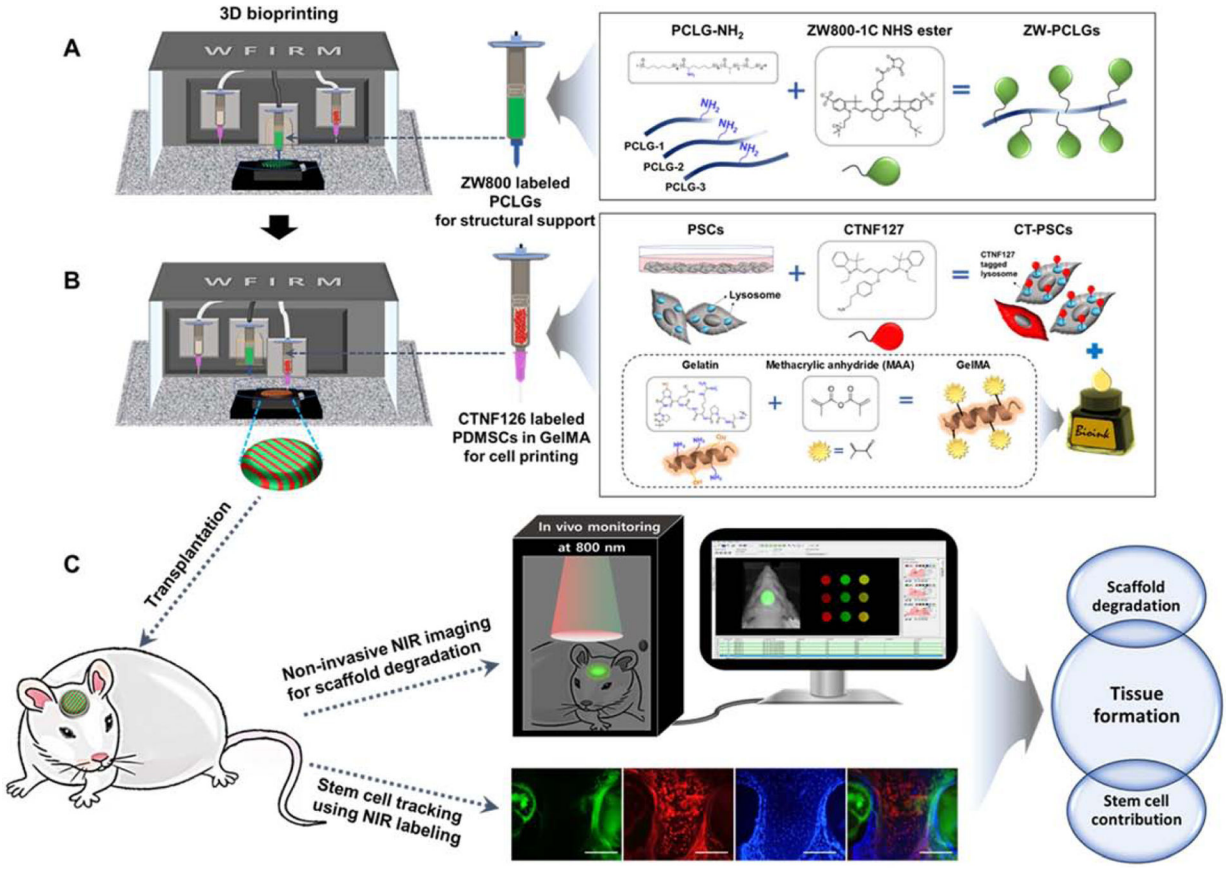

Fig. 1.

Schematic illustration of NIR imaging system for monitoring *in vivo* behaviors of polymeric scaffolds and stem cells. (A) 800-nm emitting ZW800–1C-conjugated PCLG-based scaffold (ZW-PCLGs), (B) 700-nm emitting CTNF127-labeled PSCs (CT-PSCs), and (C) NIR imaging for tracking scaffolds and stem cells after transplantation.

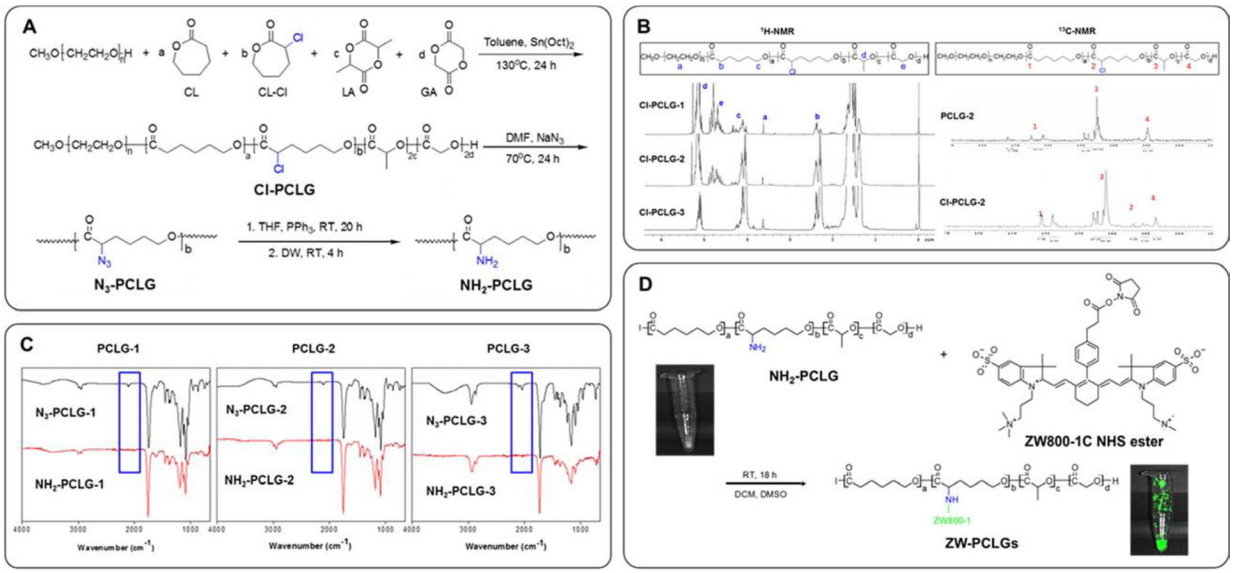

Fig. 2.

Synthesis of ZW800–1C-conjugated PCL-ran-PLLA-ran-PGA (PCLG) copolymers. (A) Scheme of copolymerization and NH -functionalized PCLGs, (B) ^{1}H-NMR and^{13} C-NMR spectra of Cl-PCLG copolymers, (C) FT-IR spectra of NH_2-functionalized PCLGs, (D) Conjugation of NHS-activated ZW800–1C ester to NH_2-functionalized PCLGs.

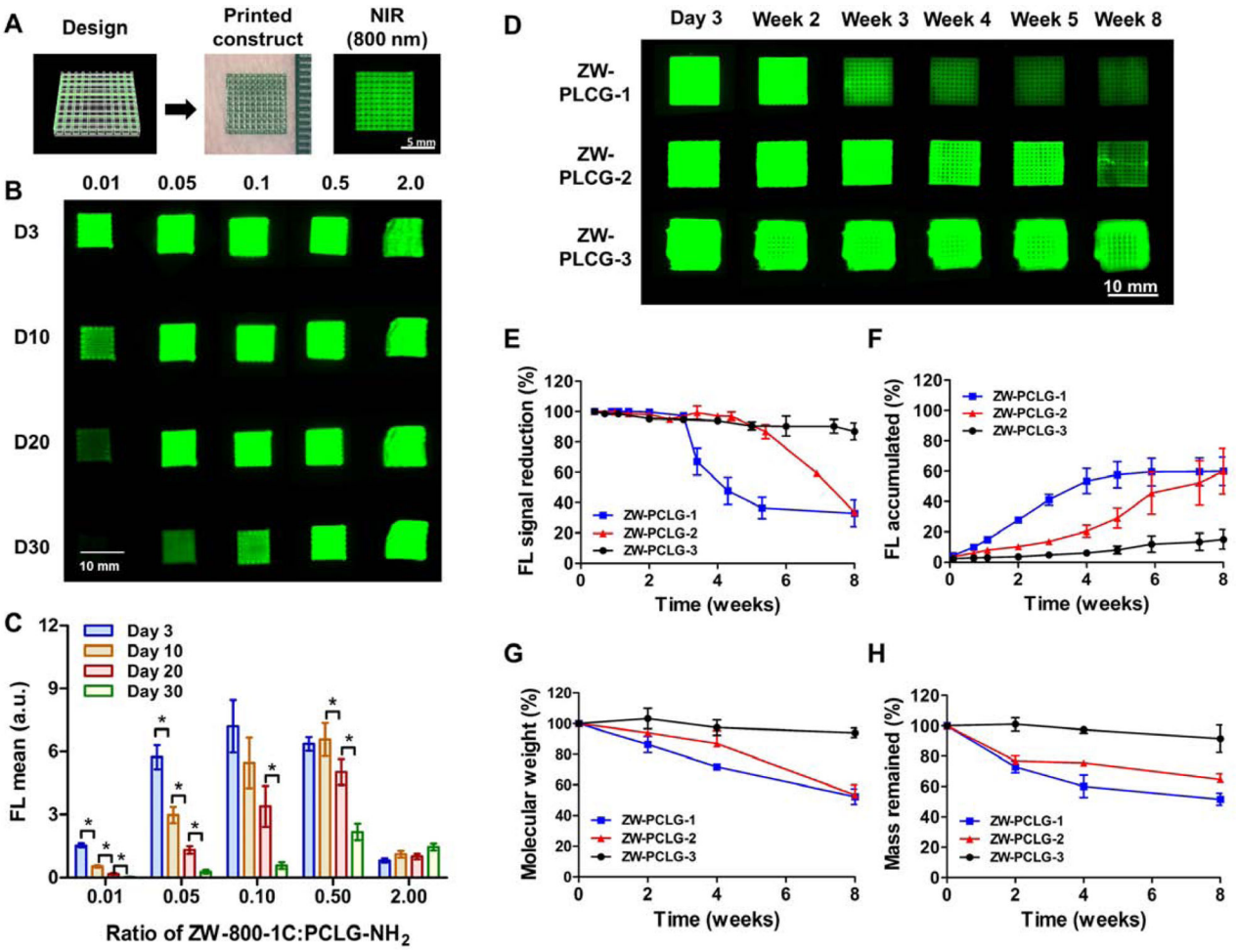

Fig. 3.

Fabrication and *in vitro* degradation testing of ZW-PCLG copolymers. (A) The ZW-PCLG scaffolds were printed based on CAD design and visualized by 800-nm emission. (B, C) Optimization of ZW800–1C:PCLG ratios for NIR-based monitoring: (B) *in vitro* NIR fluorescent images and (C) quantitative fluorescence intensity of the printed ZW-PCLG scaffolds with different ZW800–1C:PCLG ratios (0.01–2.0) under physiological condition. (D–H) *In vitro* degradation test of ZW-PLCGs with different monomer ratios: (D) NIR fluorescent images of the printed ZW-PCLG scaffolds under physiological condition. Quantification of (E) NIR fluorescence intensity remained in the scaffolds and (F) the accumulated fluorescence signal in the buffer. (G) Molecular weight changes measured by ^{1}H NMR and (H) the remained mass of the ZW-PCLG scaffolds.

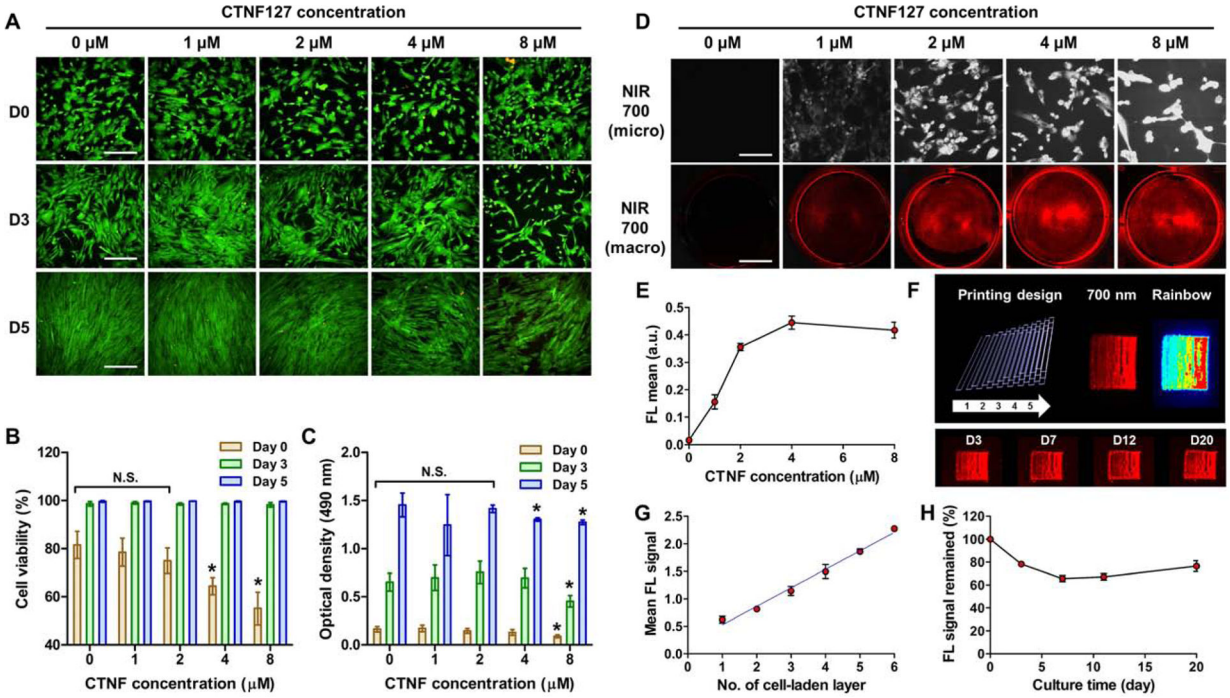

Fig. 4.

CNTF127 labeling of hPSCs for cell tracking. (A) Live/Dead stained images of hPSCs after CTNF127 treatment with different concentrations. (B) Cell viability (%) and (C) cell proliferation after CTNF127 treatment with different concentrations. (D) NIR fluorescence images of CTNF127-labeled hPSCs (CT-PSCs) with different CTNF127 concentrations (top, scale bar = 250 μm; bottom, scale bar = 1 cm). (E) Quantification of NIR fluorescence intensity with different CTNF127 concentrations. (F) The CT-PSCs-laden GelMA-based bioink was printed based on CAD design and visualized by 700-nm emission. (G) Quantification of NIR fluorescence intensity with different number of cell-laden printing layer. (H) Quantification of the remained NIR fluorescence signal in the printed CT-PSCs-laden constructs for up to 20 days in culture.

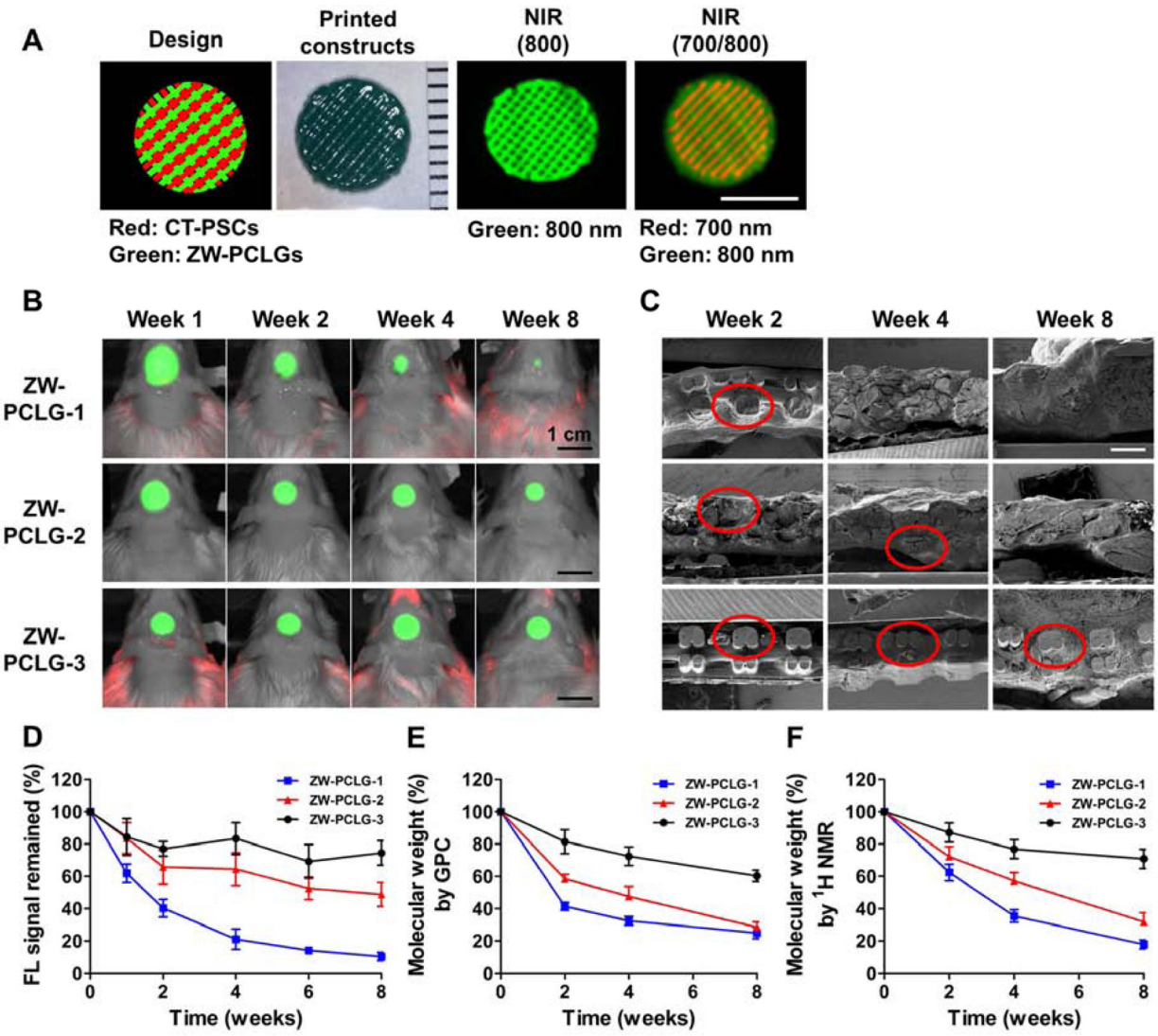

Fig. 5.

In vivo noninvasive NIR monitoring for scaffold degradation. (A) The hybrid construct containing the CT-PSCs-laden hydrogel and the ZW-PCLG was printed based on CAD design and visualized by 700-nm and 800-nm emission, respectively. Scale bar = 5 mm (B) NIR images of the ZW-PCLG scaffolds in the defected calvarial bone of rats at 1, 2, 4, and 8 weeks post-implantation. Scale bar = 1 cm (C) SEM images of the retrieved PCLG scaffolds at 2, 4, and 8 weeks post-implantation. Scale bar = 500 μm. (D) Quantification of the remained NIR fluorescent intensity in the ZW-PCLG scaffolds. Molecular weight changes measured by (E) GPC and (F) ^{1}H NMR.

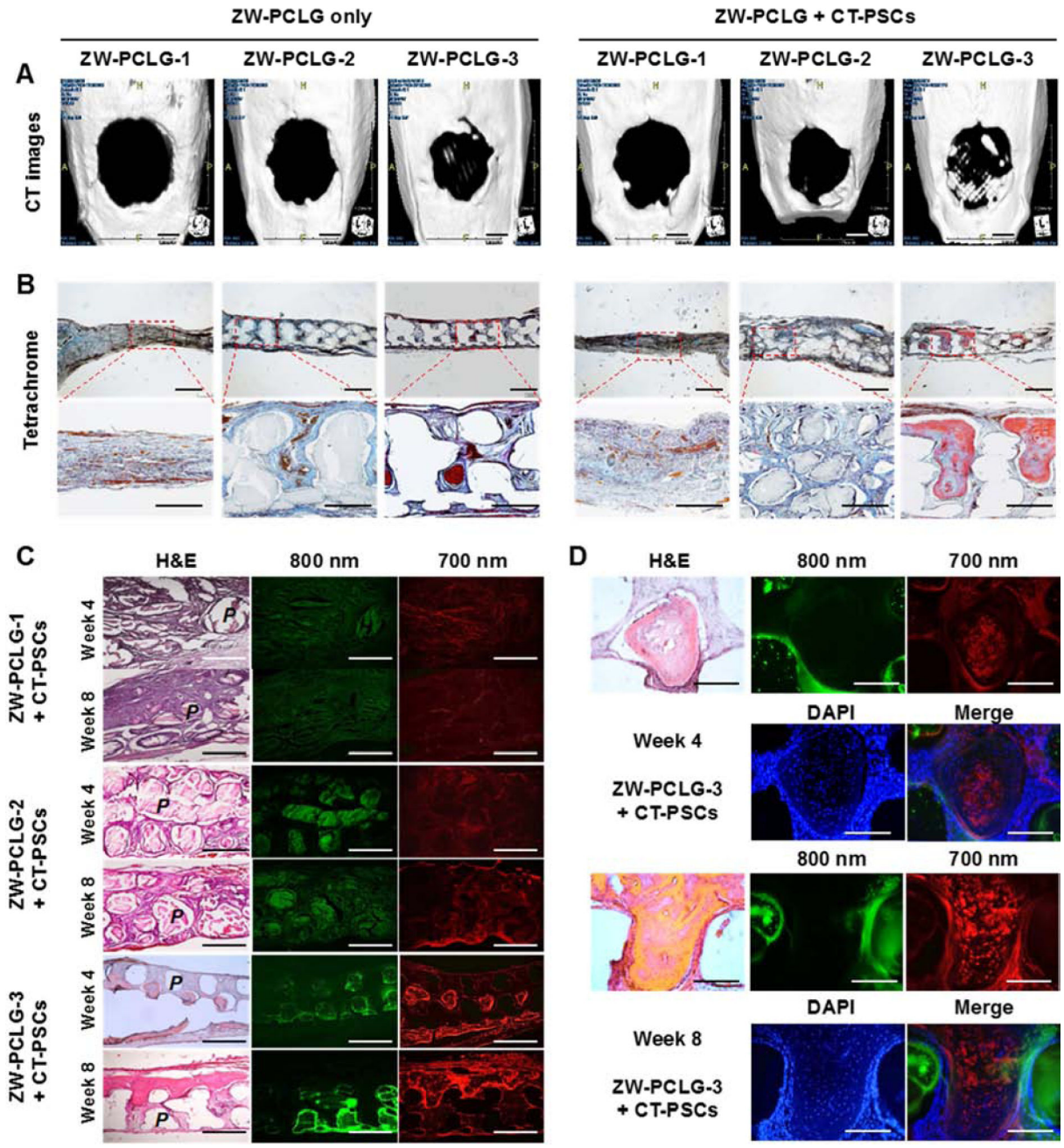

Fig. 6.

CT and histological examinations of the CT-PSCs and PCLG scaffolds. New bone formation in the calvarial bone defect was examined by (A) CT (scale bar = 2 mm) and (B) modified Tetrachrome staining (scale bar = 1 mm). (C) The remained PCLG scaffolds and hPSCs were detected by H&E staining and NIR imaging (P = PCLG). Green pseudo color at 800 nm indicates the remained PCLG scaffold, and red pseudo color at 700 nm indicates hPSCs. (D) High power images to confirm hPSCs within bone matrix in ZW-PCLG-3 + CT-PSCs. The blue color indicates DAPI-stained nuclei. Scale bar = 500 μm.

Table 1

Synthesis of PCLG copolymers by different monomer ratios.

PCLGs	[CL]/[CL-C1]/[LA]/[GA] Molar ratio[a]	Yield (%)[b]	$M_{n,\ calcd}$ (g/mol)[a]	Dispersity (Đ)[c]
$PC_{10}L_{70}G_{20}$ (PCLG-1)	10/2/68/20	98	490,000	1.9
$PC_{30}L_{60}G_{10}$ (PCLG-2)	32/2/58/10	97	520,000	2.0
$PC_{90}L_{10}G_{0}$ (PCLG-3)	88/2/10/0	98	570,000	1.6

Initiator is methoxy poly(ethylene glycol) (MPEG) (750, M_W/M_n = 1.12). Condition; [$Sn(Oct)_2$]/[Initiator] = 1.2

[a] Determined by ^1H NMR spectroscopy.

[b] *n*-Hexane/diethyl ether (4/1) insoluble part.

[c] Measured by gel permeation chromatography (GPC) (Based on standard polystyrene). CL: caprolactone, CL-Cl: chloro-caprolactone, LA: lactic acid, GA: glycolic acid.